NATIONAL UNIVERSITY of SCIENCE and TECHNOLOGY

POLITEHNICA BUCHAREST

DOCTORAL SCHOOL of ELECTRICAL ENGINEERING

EXTENDED ABSTRACT
Ph. D. THESIS

ELECTROMAGNETIC METHODS IN EXTRACTION TECHNOLOGIES FOR CERTAIN ORGANIC SUBSTANCES

Ph. D. Student:

Ing. Florin SĂFTOIU

Ph. D. Supervisor:

Prof. Dr. Ing. Alexandru-Mihail MOREGA

BUCUREŞTI
2025

Contents

Introduction 4

1.1 Presentation of the PhD topic 4

1.2 Aim of the PhD thesis 4

1.3 Content of the thesis 4

Current framework and research directions 5

2.1 Conclusions 5

Separation principles 6

3.1 Classical separation principles 6

3.1.1 Separation by sedimentation 7

3.1.2 Separation by centrifugation 7

3.1.3 Steam distillation 7

3.1.4 Liquid - liquid separation 7

3.2 Contemporary separation methods 7

3.2.1 Pulsed electric field 7

3.2.2 Microwave field 8

3.2.3 Ultrasound 8

3.3 Conclusions 8

Photovoltaic power source 9

4.1 Photovoltaic conversion 9

4.2 Solar irradiance as a power source 9

4.3 The photovoltaic converter 10

4.4 Using thermal irradiance in PV operation 10

4.4.1 An analytical estimate of thermal influx at the panel 10

4.4.2 Panel modeling 10

4.4.2.1 Mathematical model: heat-transfer problem 10

4.4.2.2 Solution S_0 – natural-convection cooling 11

4.4.3 Solution S_1 – single-stream heat exchanger 11

4.4.4 Solution S_2 – counter-flow heat exchanger 11

4.5 Optimization of the thermal-power extraction system 11

4.6 Forced-convection cooling in pulses 11

4.7 Conclusions 12

Extraction in a pulsed electric field 13

5.1 Electropermeabilization and its applications 13

5.2 Electropermeabilization at the cell level 13

5.3 Electropermeabilization in pulsed electric field 13

5.4 Model for electropermeabilization in an electric field 14

5.5 Electrical properties for lavender in the EP process 14

5.5.1 At the cell level 14

5.5.2 At the volume level 15

5.6 Numerical modeling of electropermeabilization 15
5.6.1 Sizing an electropermeabilization device 15
5.6.2 Electrical conductivity during the electropermeabilization process 16
5.6.3 Numerical modeling of the electropermeabilization cell under PWM pulses 16
5.6.4 Circular electropermeabilization cell 17
5.6.5 Elliptical electropermeabilization cell 18
5.6.6 Electropermeabilization cell with rotating electrodes 19
5.6.7 Conclusions 20
Extraction in an ultrasonic field 21
6.1 US sources used in the extraction process 21
6.1.1 Piezoelectric effect 21
6.1.2 Piezoelectric converter 22
6.1.3 Magnetostrictive converter 23
6.2 Use of US waves in extraction 23
6.3 US-assisted extraction process 24
6.3.1 Piezoelectric ultrasound source 24
6.3.2 Sonotrode analysis 25
6.3.3 Integration of the sonotrode with the extraction cell 25
6.3.3 Integrarea sonotronului cu celula de extracţie 26
6.3.4 Modeling of the processes occurring in the ultrasound extraction cell 27
6.4 Conclusions 28
Conclusions 29
7.1 Obtained results 29
7.2 Original contributions 30
7.3 Development directions 30
7.4 List of published works 31
7.5 Final conclusion 31
References (selection) 32

Chapter 1
Introduction

Research and development activities are the engine of technological progress and differentiation in today's markets, extending beyond the mere generation of knowledge to encompass product and service innovation, process improvement, and resource optimization. By integrating research outcomes into applied strategies, R&D enhances competitiveness, reduces costs, and supports sustainable solutions, thereby serving as a catalyst for industrial transformation and long-term positioning within a dynamic economic ecosystem.

1.1 Presentation of the PhD topic

This thesis presents research in electrical engineering within a multidisciplinary framework (electrical engineering, biology, technology, and economics), applied to the extraction procedures and processes for specialty coffee and essential oils. The focus is on modern electromagnetic methods that enable fine control of process parameters, thereby increasing extraction efficiency, preserving the integrity of aromatic compounds, and reducing energy costs. The research approach considers both the mechanisms of cellular permeabilization and the physiological characteristics of plant-based raw materials, as well as the economic and sustainability implications associated with industrial-scale implementation.

1.2 Aim of the PhD thesis

The thesis aims to define and evaluate high-performance, scalable, and environmentally responsible extraction processes based on electromagnetic and electromechanical technologies, powered and optimized for energy efficiency. These processes are intended to preserve compound quality while significantly reducing energy consumption, with the additional objective of ensuring the energy independence of the extraction system.

1.3 Content of the thesis

Chapter 1 presents the current general framework, the multidisciplinary context, and the main research directions.

Chapter 2 argues for the need to modernize extraction processes and positions electromagnetic-field-based technologies as viable and promising alternatives to conventional methods.

Chapter 3 presents the principles and criteria of separation from plant matrices, performance indicators, and operational windows, including case studies on lavender and coffee, and establishes the physico-mathematical basis for subsequent modeling.

With the objective of ensuring the energy independence of an extraction installation, Chapter 4 proposes a photovoltaic converter as a power source, capable of valorizing both solar irradiance and Joule losses (generated heat) within the system.

Chapter 5 addresses the modelling of electroporation in a pulsed electric field within an extraction cell, including energy recovery from solar irradiance and Joule losses.

Chapter 6 addresses ultrasound-assisted extraction using a piezoelectric sonotrode, while Chapter 7 synthesizes the conclusions, original contributions, and future directions. In all cases, implementation relies on the power source and the technological installation suited to the conversion principle.

Chapter 2
Current framework and research directions

In the context of sustainable development and the growing demand for high-quality natural products, optimizing the extraction of bioactive compounds from plant-based raw materials has become a priority. Conventional extraction methods are energy-intensive, slow, and may degrade sensitive compounds. Emerging technologies based on electric and electromagnetic fields—pulsed electric fields (PEF), microwave-assisted extraction (MAE), and ultrasound-assisted extraction (UAE)—offer intensified mass transfer with a reduced energy footprint. The scientific literature confirms the effectiveness of PEF, MAE, and UAE across various plant matrices, including coffee and species in the Lamiaceae family; however, their adoption in industrial-scale applications remains limited. A persistent gap between laboratory results and real processing lines justifies integrated approaches combining multiphysics modeling with experimental validation.

Lavender essential oil (*Lavandula angustifolia*) is characterized by high contents of linalyl acetate (25%–45%) and linalool (25%–38%), with low camphor levels (0.5%–1%), key quality indicators according to ISO standards [1]. While steam distillation remains the industrial reference, green techniques such as MAE and UAE can significantly reduce processing time and energy consumption while preserving comparable aromatic profiles [2].

Coffee is a strategic global commodity with a complex chemical composition that includes more than 1,000 bioactive compounds, including caffeine and chlorogenic acids. The sector is increasingly affected by climate change, price volatility, and the vulnerability of small producers, while trends such as Fair Trade, organic certification, diversified brewing methods, and the "Third Wave" movement emphasize quality and traceability [3].

Recent volatility in Arabica coffee prices, linked to unfavorable agroclimatic conditions in 2024, and the growth of circular valorization pathways for lavender highlight the need for flexible and robust extraction processes. With the essential oils market projected to expand rapidly through 2030, scalable and sustainable production capacities are required, in line with sustainable development principles [4]. This thesis investigates electrotechnical extraction methods (PEF, MAE, and UAE) to (i) optimize the extraction of active compounds from coffee and (ii) intensify the recovery of oils and other valuable compounds from aromatic plants such as lavender, while preserving sensitive compounds and reducing specific energy consumption.

2.1 Conclusions

The necessity of transitioning from conventional extraction methods to emerging technologies based on electric and electromagnetic fields is demonstrated. PEF, MAE, and UAE have reached a sufficient level of technological maturity to be tested as industrial solutions that directly impact both efficiency and product quality. The selection of lavender and coffee as model matrices is economically and technologically justified.

The research direction focuses on coupling multiphysics modeling with experimental validation and integrating the proposed processes into a circular valorization framework, supported by a systematic comparison of numerical simulations and experimental results.

Chapter 3
Separation principles

This chapter presents a study of the mechanisms governing the separation of elements naturally combined within materials, under the action of mechanical, thermal, electrical, or magnetic forces. The techniques addressed include thermal effects, ultrasound, microwaves, and electroporation/electropermeabilization. Some separation processes involve combined or hybrid stages, such as ultrasound-assisted thermal distillation or microwave-assisted ultrasonic separation [5].

The need for separation arises from the objective of preserving and valorizing biologically active components within mixtures or materials that are of interest for medical, pharmaceutical, nutritional, and cosmetic applications. Conventional methods, such as aqueous maceration, are slow, material- and energy-intensive, and may compromise the quality of sensitive compounds. Ultrasound-assisted processes shorten separation times via cavitation-induced disruption of cell membranes while preserving compound integrity. Alternative approaches based on electric current have also been proposed, including moderate electric fields and ohmic heating. The former promotes membrane permeabilization, whereas the latter enhances heating efficiency. Electroporation may be reversible or irreversible, depending on the field parameters, and its effects are assessed using measurements of compound flux across the membrane, electrical conductivity, and impedance. Ohmic heating can significantly reduce overall processing time.

In ultrasound-assisted extraction, commonly used solid–liquid ratios, moderate power levels, and controlled temperatures are employed, with probes immersed directly in the medium to ensure efficient energy coupling.

The common analytical framework adopted in this chapter includes transport phenomena (diffusion, convection, and migration in electric fields), phase–phase equilibria, solvent–matrix interactions, and performance indicators such as yield, selectivity, specific energy consumption, productivity, and preservation of sensitive compounds. Classical separation methods (sedimentation, centrifugation, steam distillation, and liquid–liquid separation) are compared with modern technologies based on electrical and electromagnetic principles—pulsed electric fields (PEF), microwave-assisted extraction (MAE), and ultrasound-assisted extraction (UAE)—which are employed here as extraction methods rather than pretreatments.

The applied focus remains on lavender (essential oil, hydrolate, phenolic compounds) and ground coffee (cold-brew extract), with method selection simultaneously targeting efficiency, quality, sustainability, and industrial scalability. The chapter concludes with performance indicators and design considerations that are subsequently used to model and optimize the UAE and PEF processes.

3.1 Classical separation principles

Classical separation technologies rely on differences in physical properties such as density (sedimentation), inertial forces (centrifugation), volatility and partial vapor pressures (steam distillation), and immiscibility combined with density contrasts (liquid–liquid separation). These methods are robust, well understood, and easy to implement; however, they often involve long processing times and high energy consumption, with associated risks of degrading sensitive compounds. Process selection depends on operating windows (temperature, pressure, viscosity, solid–liquid ratio), particle-size distribution, and quality objectives. At an industrial scale, standardized equipment facilitates implementation, but

energy optimization rapidly reaches a plateau, motivating the search for mass-transfer intensification through modern technologies.

3.1.1 Separation by sedimentation

Sedimentation is based on density differences between phases in a mixture. Under gravitational forces, heavier particles settle while the liquid phase remains above. This method is widely used in the pretreatment of plant-based liquids and for decantation. Separation velocity increases with particle size and density contrast and decreases with increasing medium viscosity.

3.1.2 Separation by centrifugation

Centrifugation accelerates sedimentation by applying centrifugal forces generated by rotating equipment. It is effective for liquid–solid and liquid–liquid separations, commonly used in extract purification and crude oil separation. The increased effective acceleration relative to gravity significantly shortens processing time, at the expense of higher mechanical energy input.

3.1.3 Steam distillation

Steam distillation enables the extraction of volatile compounds, such as essential oils, without reaching the high temperatures associated with direct boiling. The steam–volatile mixture boils at a lower temperature than each individual component, thereby reducing thermal degradation. A typical installation comprises a steam generator, an extraction chamber, a condenser, and a phase separator. Process yield is defined as the mass of extracted oil per unit mass of plant material, whereas steam demand can be estimated from energy balance calculations.

3.1.4 Liquid - liquid separation

The Florentine flask allows gravitational separation of two immiscible liquids, typically essential oil and hydrolate. The denser phase accumulates at the bottom, while the lighter phase remains above, with discharge occurring through separate outlets. The method is simple, effective, and requires no additional energy input.

3.2 Contemporary separation methods

This work analyzes three modern separation methods that exploit electrical and electromagnetic principles to enhance the release of bioactive compounds from plant matrices: pulsed electric fields (PEF), microwave-assisted extraction (MAE), and ultrasound-assisted extraction (UAE). These techniques are characterized by high efficiency, short processing times, and improved preservation of sensitive compounds.

3.2.1 Pulsed electric field

PEF involves applying high-voltage pulses directly to a sample positioned between electrodes in the presence of a food-grade solvent. The applied electric field electropermeabilizes cell membranes, reduces mass-transfer resistance, and enhances intracellular diffusion into the solvent. Critical parameters include field strength, pulse duration and number, specific energy input, medium conductivity, temperature, and solid–liquid ratio.

Advantages include reduced extraction time, lower solvent and energy consumption, and preservation of thermosensitive compounds. Limitations arise at low conductivities due to field and thermal non-uniformities and stringent requirements for reactor design and thermal

control. For lavender and coffee matrices, the method is promising provided that specific energy input and cell geometry are carefully optimized.

3.2.2 Microwave field

Microwave-assisted extraction (MAE) exploits dielectric heating of water and polar solvents, enabling rapid volumetric heating, increased intracellular pressure, and the concurrent expulsion of cellular contents into the solvent during extraction. Variants such as solvent-free extraction and gravity-driven hydrodiffusion are widely used for essential oils and significantly reduce processing times compared with conventional distillation while maintaining aromatic profiles.

Precise power control is essential to avoid hot spots and localized degradation. Extraction yield depends on the solvent type, solid–to–liquid ratio, applied power, processing time, and temperature, with polar solvents exhibiting greater energy absorption. In applications involving lavender and coffee, MAE achieves yields comparable to conventional methods within substantially shorter timeframes.

3.2.3 Ultrasound

Ultrasound-assisted extraction (UAE) employs ultrasonic waves that induce acoustic cavitation, generating microjets and localized shear forces that fragment cell walls and intensify mass and heat transfer. Key control parameters include ultrasonic power or amplitude, frequency, temperature, solid–liquid ratio, and probe or bath geometry. Advantages include reduced processing time, lower solvent consumption, moderate operating temperatures, and protection of sensitive compounds. Limitations include the risk of oxidation or isomerization under intense cavitation and the formation of localized overheated zones, necessitating thermal control and, where appropriate, inert atmospheres. For lavender and coffee, UAE reduces processing times from hours to minutes while achieving performance comparable to conventional extraction methods.

3.3 Conclusions

This chapter established a common analysis framework for separation technologies applicable to plant matrices, balancing the robustness of classical methods with the speed and efficiency of field-based technologies. Sedimentation, centrifugation, steam distillation, and liquid-liquid separation remain core, scalable steps, but often involve long processing times, high energy costs, and risks for sensitive compounds. By contrast, pulsed electric fields, microwaves, and ultrasound reduce transfer barriers at the cellular level through electroporation, volumetric dielectric heating, and acoustic cavitation, accelerating compound release, shortening durations, and often reducing solvent and energy use while preserving quality. The specific limitations of each technology require fine control of energy, reactor/cell design, and thermal conditions.

For lavender and coffee, the results support modern or hybrid routes in which classical operations (e.g., condensation, decantation) remain post-treatments, whereas release/transfer is intensified by fields. Method choice depends on product target, matrix, and solvent properties, and acceptable operating constraints. The comparative analysis justifies the use of numerical modeling for PEF and UAE multiphysics processes that are sensitive to the space-time distribution of energy and to technological geometry details, thereby reducing experimental cycles and the risk of compound degradation.

Chapter 4
Photovoltaic power source

In the context of electrically assisted extraction processes (*e.g.*, pulsed electric fields [PEF] and ultrasound-assisted extraction [UAE]), the power supply plays an essential role in the installation's portability, sustainability, and energy control. Photovoltaic conversion provides a direct solution for supplying the electrical generators used in extraction, thereby eliminating dependence on conventional grids and integrating the process into an autonomous energy architecture.

Moreover, the electromagnetic nature of PV conversion is conceptually compatible with the extraction processes studied, in which electric fields and delivered energy govern matrix permeabilization, mass transfer, and extraction yield. Therefore, the photovoltaic source is not treated merely as a supply element, but as an integral part of a coherent energy chain oriented toward sustainable, scalable extraction processes with a reduced energy footprint.

4.1 Photovoltaic conversion

Solar energy is a renewable resource with significant potential to replace or supplement conventional energy sources. Photovoltaic (PV) technologies convert solar energy directly into electricity via the photovoltaic effect.

A PV system comprises solar panels (mono- or poly-crystalline silicon cells or thin-film technologies), an inverter, a charge controller (with maximum power point tracking, MPPT), batteries, mounting structures, and cabling.

In the context of climate change and the transition to “green” energy sources, PV systems are relevant to both large-scale applications and mobile or laboratory systems (sensors, portable devices, and extraction and processing equipment).

Key advantages include energy independence, reduced carbon footprint, operation in remote areas, and sustainable powering of low-consumption equipment. In this work, PV sources are analyzed as power sources for extraction equipment (*e.g.*, PEF/UAE) to enable sustainable, mobile, and scalable processes.

System sizing is correlated with the load power demand (*e.g.*, a 200 W ultrasound generator [19]), daily operating time, local irradiance, storage/autonomy requirements, and inverter and control efficiencies.

4.2 Solar irradiance as a power source

Electromagnetic radiation is one of the three heat-transfer mechanisms and is the primary source of energy for photovoltaic panels. Unlike conduction and convection, radiation requires no material medium for propagation, enabling Sun–Earth energy transfer.

The phenomenon can be described both within classical electromagnetism (continuous media, wave hypothesis for the electromagnetic field) and within quantum theory (corpuscular hypothesis of discrete energy packets—photons). The visible portion of the electromagnetic spectrum is relevant to PV conversion, whereas the infrared (IR) component contributes to PV cell overheating. Thermophotovoltaic cells dedicated to IR conversion also exist [24].

In PV conversion, emissivity, absorptivity, reflectivity, and transmissivity characterize electromagnetic field–cell (matrix) interactions [6]. Incident solar irradiance is attenuated by the atmosphere, and the assessment of useful fluxes (direct and reflected irradiance) accounts for solar geometry (azimuth, altitude/zenith) as well as panel position and orientation. High-

precision solar positioning algorithms may be used to determine solar angles. These elements provide the basis for the analytical and numerical models employed later [7].

4.3 The photovoltaic converter

Photovoltaic conversion transforms the electromagnetic wave (photons) directly into electrical energy at the p–n junction of the PV cell. The outer anti-reflective coating, transparent/conductive contacts, and the semiconductor material (mono-Si, poly-Si, a-Si, CdTe, CIGS, etc.) significantly influence conversion efficiency.

Common electrical parameters include the voltage and current at the maximum power point (Vmp, Imp), maximum power at MPP (PMPP), fill factor (FF), and efficiency (η).

Temperature is a critical factor: as the panel heats (IR absorption, Joule losses under load, and ambient conditions), efficiency decreases. Cooling strategies can be implemented using passive solutions (*e.g.*, ceramic vessels, the thermosiphon effect) and active solutions (hydraulic loops with pumps, thermal collectors with controllable I/O ports, rear-side pipes/coils, counter-flow arrangements). Performance depends on geometry, flow rate, flow distribution, and energy integration [8]. This subsection analyzes both thermal loading effects and options for valorizing extracted heat in a secondary energy-conversion circuit (PV/T configurations).

4.4 Using thermal irradiance in PV operation

4.4.1 An analytical estimate of thermal influx at the panel

The panel is modeled as a plate heated by standard solar irradiance and cooled by natural convection to ambient air. Isothermal/isoflux operating conditions are assumed for the exposed face of the PV panel, and the influence of panel tilt on cooling is analyzed [9]: at large angles (relative to vertical), the convective heat-transfer coefficient decreases, and natural cooling is reduced.

The analytical results provide orders-of-magnitude magnitude estimates for the operating temperature and the convective heat-transfer coefficient. These data can serve for preliminary thermal pre-sizing of the PV converter and are later verified and confirmed through numerical modeling. Conclusion: optimal panel positioning (tilt angle) improves passive cooling, but for specific thermal loads, an active cooling scheme is required.

4.4.2 Panel modeling

The analysis indicates that, by implementing a water-cooling system under forced-flow conditions, usable thermal power can be extracted—potentially through an additional thermodynamic cycle—while maintaining the operating temperature within optimal limits, thereby increasing overall energy efficiency (PV/T configuration) [10].

4.4.2.1 Mathematical model: heat-transfer problem

Two families of cooling solutions are proposed and analyzed to maintain PV thermal stability: natural convection (passive thermal stability) and forced convection (stability plus thermal power extraction for a secondary cycle), using water as the working fluid. For forced convection, the efficiency of a single-coil design (single-stream) is compared with that of a counter-flow cooling architecture.

Flow in the rear heat exchanger is assumed steady, viscous, incompressible, laminar or turbulent, single-phase (below the boiling point), governed by the Navier–Stokes equations (momentum and mass conservation) for a Newtonian fluid. Boundary conditions include an inlet velocity profile, outlet pressure, and no-slip walls. The heat-transfer problem is described

by the energy equation (the first law of thermodynamics). Internal heat sources include Joule losses (from panel operation under load) and an equivalent heat input associated with incident IR irradiance.

Thermal boundary conditions include a convective heat-flux (power) condition at the rear side, thermal insulation at the frame, and an imposed coolant inlet temperature [10]. Both models are formulated here in a steady state.

4.4.2.2 Solution S_0 – natural-convection cooling

For natural cooling (without forced-flow cooling), the PV panel temperature distribution is quasi-uniform but elevated. Passive cooling depends on tilt angle: the convective coefficient decreases at large angles, whereas the thermal load increases with the extracted electrical power. The numerical results confirm the earlier analytical predictions. Conclusion: natural convection alone is insufficient to maintain PV efficiency under real operating conditions [10].

4.4.3 Solution S_1 – single-stream heat exchanger

With a single coil and forced flow, the panel becomes nearly isothermal at lower temperatures. Increasing the flow rate (inlet velocity) enhances cooling and reduces panel temperature. Considering overall efficiency (including the power required to operate the hydraulic system), at high flow rates, the efficiency tends to decrease at relatively large velocities due to increased hydraulic cost. This proposed solution is therefore a good compromise between cooling performance, extracted thermal power, and pump mechanical work [10].

4.4.4 Solution S_2 – counter-flow heat exchanger

The counter-flow architecture further homogenizes the thermal field and maximizes heat extraction, yielding the lowest panel temperatures and a slight increase in P_{MPP} compared with S_1. The trade-off is approximately double the pumping effort relative to a single-coil design [11].

4.5 Optimization of the thermal-power extraction system

If the main objective is maximum electrical efficiency and heat valorization, solution S_2 (counter-flow) is recommended. If the aim is to reduce auxiliary power while maintaining moderate active cooling, solution S_1 offers similar performance with approximately half the energy consumption of S_2. The choice depends on thermal integration, pumping constraints, mass/volume limitations, and operating conditions.

4.6 Forced-convection cooling in pulses

For cases in which the coolant energy is not continuously valorized, a “pulsed” regime derived from solution S_1 is proposed, controlled by two PV panel temperature thresholds that trigger pumping initiation and cessation [11]. Numerical modeling considers the transient formulation of the energy equation.

Coolant temperature (a thermally “fresh” fluid volume) influences the cooling cycle: the panel exhibits high thermal inertia, so during each pulse (until the fluid packet is replaced), the coolant accumulates heat. This pulsating regime reduces hourly pumping power, keeps the panel at higher temperatures, and results in lower heat extraction. This solution becomes useful when the priority is simplification and minimal auxiliary consumption rather than optimization of PV/T efficiency [11].

The continuous regime (S_2) keeps the panel cool and maximizes the extracted heat at a high pumping cost; S_1 represents a compromise; and the “Pulse” regime drastically reduces auxiliary energy use but entails electrical and thermal penalties from an energy standpoint [11].

4.7 Conclusions

This chapter analyzed existing and proposed solutions, demonstrating that integrating photovoltaic conversion as a power supply for extraction equipment is feasible, provided that thermal loading is managed and the thermal stability of the PV converter (panel) is ensured. The panel operates simultaneously as an electrical generator and a “hot plate”; increasing temperature reduces efficiency, so the architecture must be treated as a PV/T system.

Natural cooling contributes, but is insufficient under real operating regimes. Forced cooling with a single coil (S_1) provides a good compromise between performance and auxiliary consumption; counter-flow (S_2) maximizes overall performance when the extracted heat is valorized. The pulsed regime minimizes pumping energy but penalizes P_{MPP} and thermal recovery.

In practice, sizing withbegins from equipment demand (*e.g.*, 200 W UAE), local irradiance, and autonomy requirements, while the cooling strategy is selected based on whether extracted heat is utilized and the system’s energy constraints.

Chapter 5
Extraction in a pulsed electric field

This chapter presents pulsed electric field (PEF)–assisted extraction, including its applications; electropermeabilization (EP) at the cellular level; electropermeabilization in a pulsed electric field; the mathematical model; the electrical properties of lavender during the EP process; numerical modeling; and conclusions.

5.1 Electropermeabilization and its applications

Electropermeabilization (EP) creates transmembrane pores that increase cell membrane permeability, thereby facilitating the release of intracellular compounds.

Modern extraction technologies such as PEF, UAE, and MAE rely on the introduction of a directed form of energy into the system to intensify mass transfer by directly modifying the cellular barrier. In PEF, electric pulses induce membrane permeabilization. In the UAE, ultrasonic waves induce acoustic cavitation, thereby generating mechanical stress and local turbulence. In MAE, electromagnetic radiation at microwave frequencies induces volumetric heating of the material, thereby increasing internal pressure and leading to cell wall rupture. Thus, each method operates through a distinct physical mechanism, yet they converge on the same objective: rapid and efficient release of target compounds with minimal alteration of organoleptic and functional properties.

EP applications include genetic transformation, microbial inactivation, and low-temperature pasteurization, and electro-extraction of biomolecules (DNA, proteins, lipids). Within the framework of modern extraction technologies, PEF acts directly on the cellular barrier, complementing ultrasound (cavitation) and microwaves (volumetric heating) [12].

5.2 Electropermeabilization at the cell level

The surface (transmembrane) voltage plays an important role in the EP process. The greater the number and diameter of pores, the smaller the membrane voltage drop becomes [136]. The distribution of membrane pores is directly proportional to the membrane voltage drop induced by the electric field, decreasing from approximately 80 mV in the refractory state to 0 mV within approximately 1–2 μs [30]. At the same time, pore resealing occurs almost instantly upon cessation of electroporation.

The impact of electric pulse shape on cell-membrane permeabilization is essential for introducing molecules into cells via EP. Pulse type—unipolar, bipolar, sinusoidal, or triangular—and the duration during which the pulse amplitude exceeds a critical threshold are crucial for permeabilization efficiency [31]. Results show that bipolar rectangular pulses are the most efficient at permeabilizing the cell membrane at lower electric-field amplitudes, whereas dynamic pulse features, such as rise and fall times, do not have a significant impact. This conclusion supports the theory that permeabilization is based on pore formation in the cell membrane and depends on the duration and intensity of the applied electric field.

5.3 Electropermeabilization in pulsed electric field

Electroporation, or electropermeabilization, occurs under the action of an electric field when the cell transmembrane electric potential exceeds a critical threshold corresponding to a limiting value of the electric-field intensity. The onset of electroporation depends on the electric-field distribution, which in turn depends on the material's electrical properties.

A phenomenon associated with the presence of an electric field in a conducting medium is the Joule effect, which causes heating of the cell membrane and promotes pore formation. Applying a pulsed electric field—pulses or pulse pairs ("bursts") at a given frequency—modifies the thermal state of the cell. Numerical simulations have shown that, up to a certain frequency, frequency and temperature are directly proportional; however, beyond that frequency, temperature decreases. Therefore, the frequency–temperature function for electroporation with pulse pairs is not monotonic [13].

5.4 Model for electropermeabilization in an electric field

Modeling the electropermeabilization (EP) process is a dynamic, non-stationary diffusion problem governed by electromagnetic field laws. The governing equations are given by Maxwell's equations and the corresponding material laws:

$$\mathrm{rot}\mathbf{E} = -\frac{\partial \mathbf{B}}{\partial t}, \quad \text{the law of electromagnetic induction,} \tag{1}$$

$$\mathrm{div}\mathbf{J} = 0, \quad \text{the law of conservation of electric charge,} \tag{2}$$

$$\mathbf{J} = \sigma(\mathbf{E})\mathbf{E}, \quad \text{the law of electrical conduction,} \tag{3}$$

$$\mathrm{rot}\mathbf{H} = \mathbf{J} + \mathbf{J}_d, \quad \text{the law of the magnetic circuit,} \tag{4}$$

$$\mathrm{div}\mathbf{B} = 0, \quad \text{the law of magnetic flux conservation,} \tag{5}$$

$$\mathbf{B} = \mu_0\mathbf{H}, \mathbf{D} = \varepsilon\mathbf{E} \quad \text{material laws for the magnetic and electric fields, respectively.} \tag{6}$$

where $\mathbf{E}$ [V/m] is the electric field intensity, $\mathbf{B}$ [T] is the magnetic flux density, $\mathbf{J}$ [A/m²] is the electric conduction current density, $\mathbf{J}_d = \partial\mathbf{D}/\partial t$ is the displacement current density, $\sigma(\mathbf{E})$ [S/m] is the electric conductivity, $\mathbf{H}$[A/m] is the magnetic field intensity, μ_0 [H/m] is the magnetic permeability, and ε [F/m] is the electric permittivity.

The electric permittivity and conductivity are assumed to be invariant in time, but dependent on the state of the organic material—non-permeabilized or permeabilized. A critical electric-field intensity (or electric potential gradient), E_{crit}, is introduced, above which the electrical conductivity undergoes a significant increase due to membrane permeabilization.

Under the operating conditions and frequencies considered, the displacement current density is negligible compared to the conduction current density. Consequently, the mathematical model of electropermeabilization in a pulsed electric field, described by equations (1)–(6), reduces to the following partial differential equation [22]:

$$-\nabla \cdot \left(\varepsilon \frac{\partial V}{\partial t}\right) - \nabla \cdot [\sigma(-\nabla V)\nabla V] = 0. \tag{7}$$

where V [V] is the electric potential.

5.5 Electrical properties for lavender in the EP process

5.5.1 At the cell level

For a plant cell (lavender), the cell diameter typically ranges from approximately 20 μm to 100 μm, the membrane thickness from about 5 nm to 8 nm, and the cell wall thickness from approximately 0.1 μm to 1 μm [29]. The reversible electropermeabilization, the critical applied voltage U_{crit} voltage lies between 0.2 V and 0.5 V, while the critical transmembrane voltage drop is approximately 1 V. The corresponding critical electric field intensity ranges from $E_{crit} = 10^6$ V/m to 10^7 V/m [29].

In continuous medium models at the membrane level, pore opening increases local electrical conductivity and reduces effective permittivity, while the cytoplasm remains highly polarizable. Essential oil exhibits a low relative permittivity [29].

5.5.2 At the volume level

Modeling material properties at the scale of a continuous medium—from nanomaterials to biological systems such as cells or soils, where interfaces separate regions with distinct electrical characteristics—can be achieved using a Maxwell–Wagner-type model [14].

$$\varepsilon_{efectiv} = \varepsilon_m \left[1 + 2\varphi \frac{\varepsilon_p - \varepsilon_m}{\varepsilon_p + 2\varepsilon_m}\right] \Big/ \left[1 - \varphi \frac{\varepsilon_p - \varepsilon_m}{\varepsilon_p + 2\varepsilon_m}\right], \quad \sigma_{efectiv} = \frac{\sigma_i \varepsilon_m \sigma_i \varepsilon_m + \sigma_m \varepsilon_p}{\varepsilon_p + \varepsilon_m}, \tag{8}$$

where φ is the volumetric fraction of the inclusions (lavender cells), ε_m is the permittivity of the surrounding medium, and ε_p is the permittivity of the inclusion (cell, particle). After electropermeabilization, the effective electrical conductivity increases, while the effective permittivity decreases, reflecting the loss of the membrane's capacitive character. The critical electric-field threshold at the working-cell level depends on geometry, electrode spacing, frequency, and material properties [28]. The critical voltage is given by

$$U_{critic} \approx A\varepsilon_r{}^{\alpha} \left(\frac{D}{d}\right)^{\beta}, \tag{9}$$

where $A \approx 15$ kV is a material constant, and $\alpha \approx 0.3$ and $\beta \approx 0.8$ are empirical exponents.

5.6 Numerical modeling of electropermeabilization

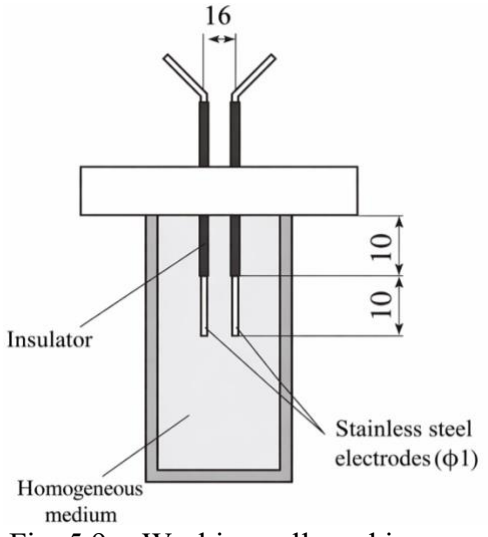


Fig. 5.9 - Working cell used in numerical modeling [25].

In the following, two fundamental stages of the electropermeabilization process are analyzed: the permeabilization stage, which takes place in the presence of the electric field, and the pore-closure stage, which occurs after removal of the electric field. The computational domain represents a volume of biological material, assumed to be heterogeneous and homogeneous by portions, corresponding to the two phases—permeabilized and non-permeabilized [25].

The working cell is a vessel pr equipped with a pair of electrodes (Fig. 5.9). Cell sizing for EP is carried out for an electrode spacing of approximately 16 mm, PWM voltage drop $V \approx 6$ V ($E_{avg} = V/d \approx 375$ V/m), PWM period 5 ms, pulse duration 50 µs, with $\sigma_{init} = 0.01$ S/m (initial, non-permeabilized state), $\sigma_{max} = 0.2$ S/m (final, permeabilized state).

5.6.1 Sizing an electropermeabilization device

The two phases—permeabilized and non-permeabilized—exhibit different electrical properties [154]. Considering the final state, when the organic material is permeabilized, the working volume can be regarded as a fluid conductor with a resistance R_c,

$$R = \frac{L}{A\sigma_{ef}}, \tag{10}$$

which galvanically closes the circuit between the two electrodes. Here, the index c denotes the mixture, solution, or organic material; L [m] is the distance between electrodes, A [m²] is the electrode contact area, and σ_{ef} [S/m] is the electrical conductivity of the organic material.

In steady-state conditions (electrokinetic, direct current), the effective electrical conductivity of the organic material is given by

$$\sigma_{ef} = \frac{I}{U}\frac{L}{A}, \tag{11}$$

where I [A] is the electric current, U [V] is the voltage applied across the electrodes, and A [m²] is the contact area between the organic mixture solution and the electrode.

5.6.2 Electrical conductivity during the electropermeabilization process

The evolution of the EP process oscillates between permeabilization of the material, with fast pore-opening rates, and pore sealing, with slower rates, depending on the duration of the PWM signal. If the local threshold condition $E > E_{crit}$ is met, pore opening occurs; during the "off" interval of the PWM period, this threshold condition is no longer satisfied.

To model this behavior, electrical conductivity is defined by

$$\frac{\partial \sigma}{\partial t} = \left[k_{open}(\sigma_{max} - \sigma)\theta(E - E_{crt}) - k_{close}(\sigma - \sigma_{initial})\right], \tag{12}$$

where k_{open} represents the pore-opening rate (0.1 s^{-1}), k_{close} represents the pore-closing rate (0,05 s^{-1}), and Θ is the Heaviside function.

The duration of the EP process is determined by the evolution of electrical conductivity, whose asymptotic exponential behavior is given by

$$\sigma(t) = \sigma_{max} + (\sigma_{initial} - \sigma_{max})e^{-\frac{k_{open}+k_{close}}{t}}. \tag{13}$$

5.6.3 Numerical modeling of the electropermeabilization cell under PWM pulses

Numerical modeling of the electropermeabilization cell under PWM pulses involves a plane section parallel to the assembly and solves, using the finite element method, the electric field subject to imposed electrode potentials (PWM signal and mass inertia). The evolution of the biological mass conductivity depends on the critical value of the electric-field intensity (pore opening and sealing). Heat transfer is considered with Joule heating as an internal source, under the assumption of a linear, homogeneous, and isotropic medium [26].

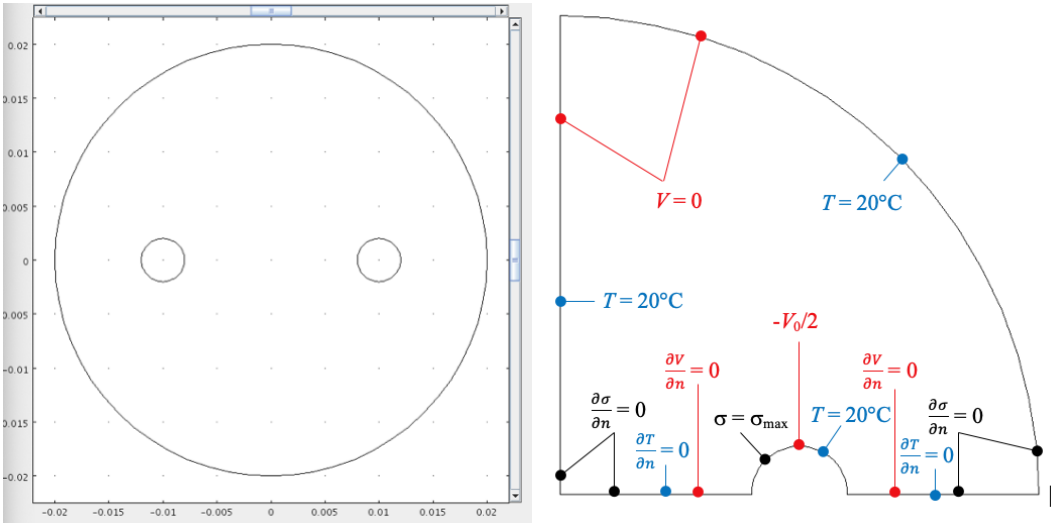


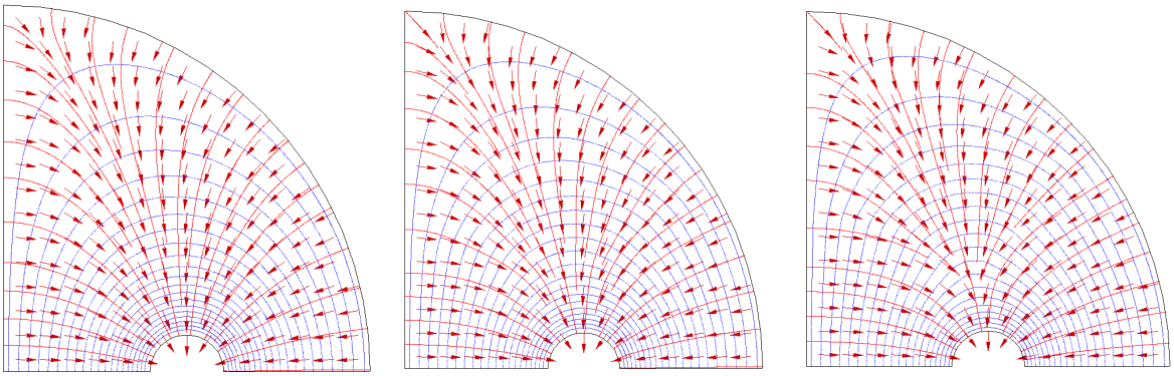
Fig. 5.10 – Boundary conditions applied to the electromagnetic field and heat transfer problems.

It is assumed that the electrodes and the cell wall are in contact with a thermostat, which maintains the temperature at 20 °C. One possible solution is the use of Peltier elements, which can remove the heat generated during electropermeabilization. The initial thermal state is T = 20 °*C*.

The solution of the three coupled "physics"—the electric field, the variation of electrical conductivity as a function of electric-field intensity, and heating—is performed simultaneously using a segregated solver [27].

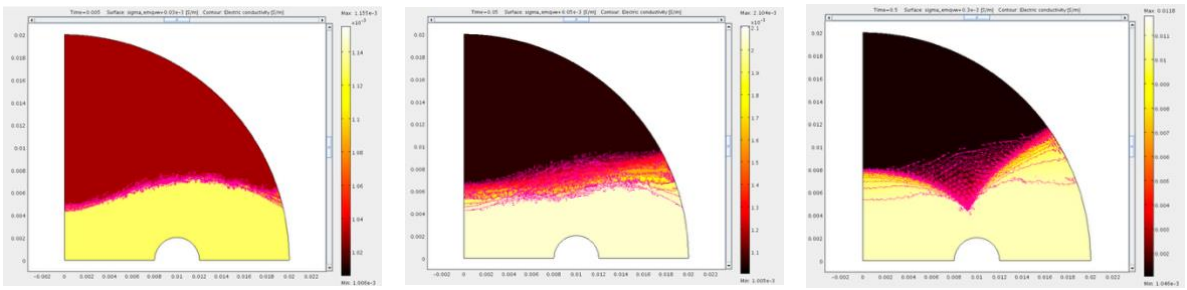
5.6.4 Circular electropermeabilization cell

The electric field exhibits persistent "sub-threshold" regions that do not undergo permeabilization for the selected parameters. Increasing the applied voltage could reduce these regions, but at the expense of increased Joule heating. With stabilized cooling, the thermal regime remains nearly isothermal at low temperatures [15].



t = 0,005 s. t = 0,05 s. t = 0,5 s.

Fig. 5.12 – Numerical simulation results showing the electric field represented by field lines and normalized vectors (electric field intensity), together with equipotential curves, for the circular cell.



t = 0,005 s. t = 0,05 s. t = 0,5 s.

Fig. 5.13 – Numerical simulation results showing the electrical conductivity distribution (color map). The EP threshold is 200 V/m.

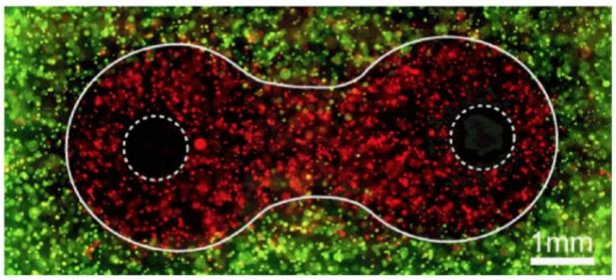
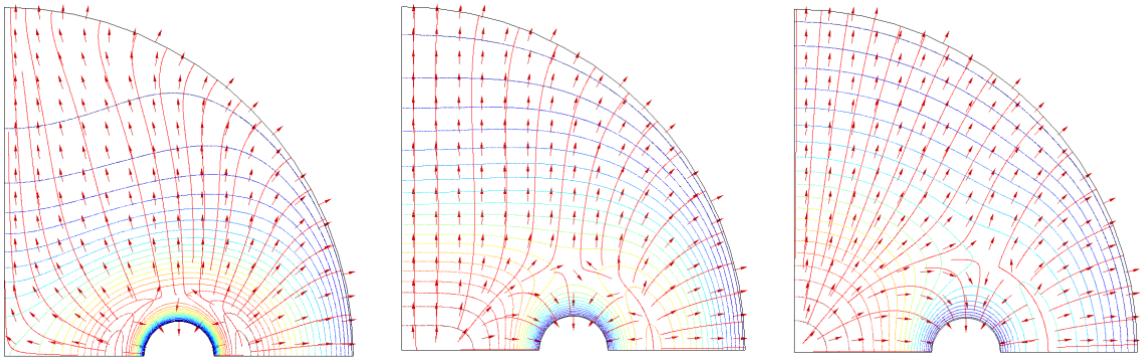


Fig. 5.14 – Cell distribution after the application of 45 pulses. Red – electropermeabilized cells; green – non-permeabilized cells [25].

The electrical conductivity distribution allows comparison of the numerical results with experimental data reported in the literature (Fig. 5.14). The white contour shown here marks the interface between the two regions, namely the permeabilized region and the still non-permeabilized region.

By correlating the electrical conductivity map (Fig. 5.13) with the electric field distribution map

(Fig. 5.12), the persistence of a region in which permeabilization does not occur during the simulation can be observed. In this region, the electric field intensity, under the established numerical modeling parameters, does not exceed the EP threshold.



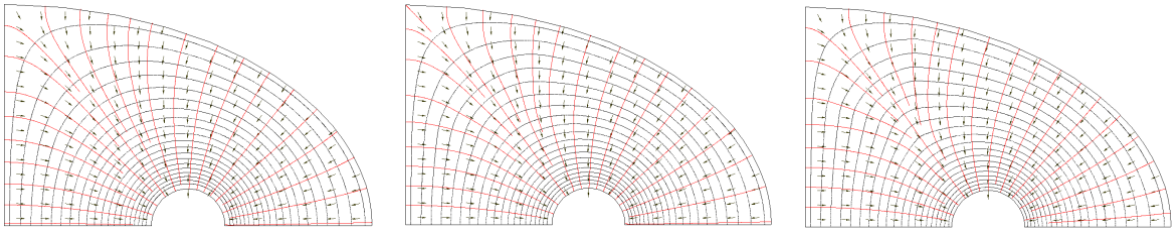
t = 0,005 s. t = 0,05 s. t = 0,5 s.

Fig. 5.15 – Numerical simulation results: thermal state of the cell, showing isothermal curves, field lines, and normalized vectors of heat-flux density (thermal power).

After 0.5 s, the cell is practically isothermal, within the range 20 °C–20.3 °C, indicating that the temperature control provided by the thermostating system ensures proper operation.

5.6.5 Elliptical electropermeabilization cell

Changing the cross-section to an elliptical shape leads to a more favorable electric-field distribution and reduces "sub-threshold" regions, thereby increasing the useful permeabilized volume without inducing undesirable thermal effects [15].

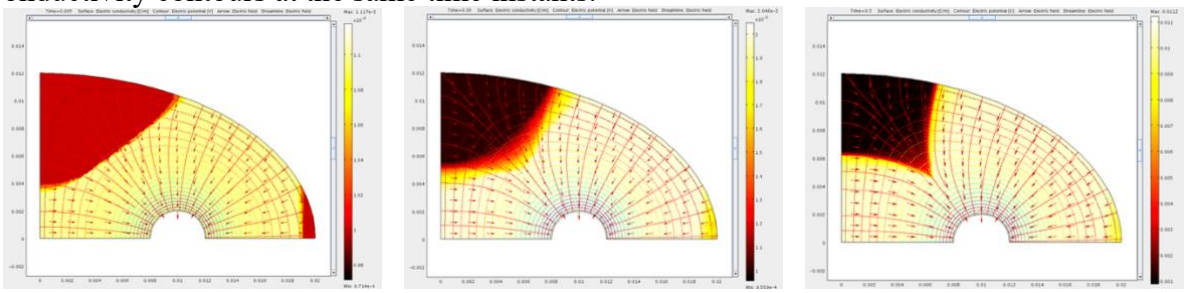


t = 0,005 s. t = 0,05 s. t = 0,5 s.

Fig. 5.16 – Numerical simulation results: electric field represented by field lines and normalized vectors (electric field intensity), together with equipotential curves. Elliptical cell.

The threshold electric-field intensity for the onset of EP is 200 V/m.

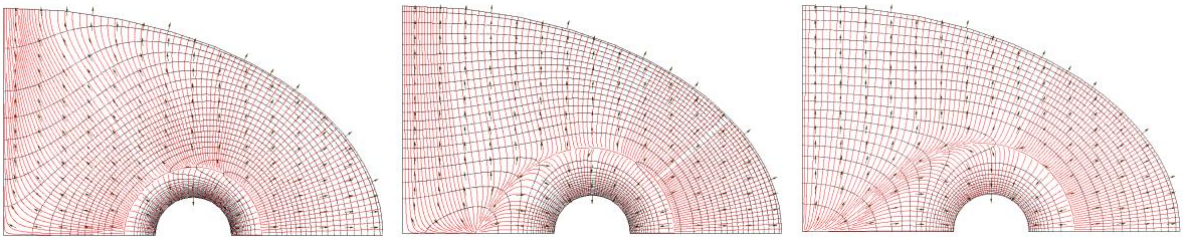
Figure 5.17 illustrates the dynamics of electrical conductivity using color maps and iso-conductivity contours at the same time instants.



t = 0,005 s. t = 0,05 s. t = 0,5 s.

Fig. 5.17 – Numerical simulation results: electrical conductivity distribution (color map). The EP threshold is set at 200 V/m.

The thermal state of the cell is shown in Fig. 5.18. After 0.5 s, the cell is practically isothermal, within the range 20 °C–20.8 °C.

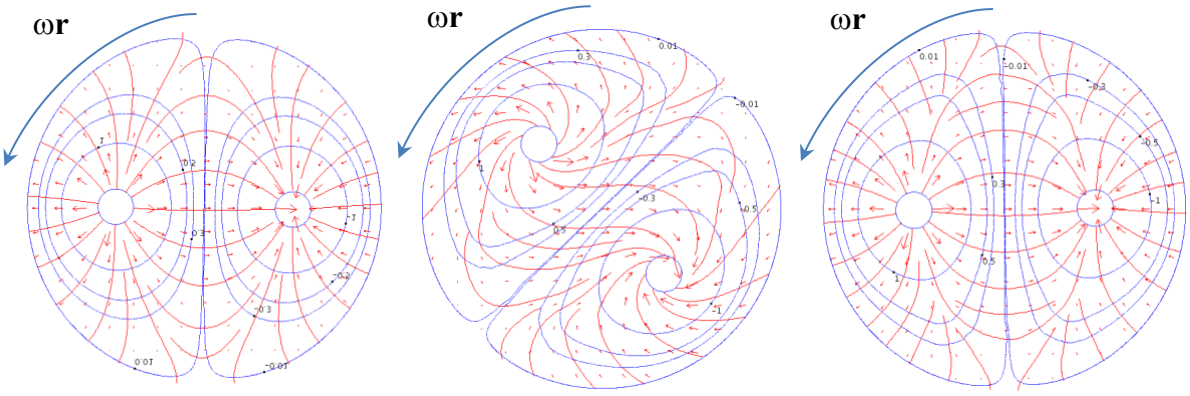


t = 0,005 s. t = 0,05 s. t = 0,5 s.

Fig. 5.18 – Numerical simulation results: thermal state of the cell, showing isothermal curves, field lines, and normalized vectors of heat-flux density (thermal power).

5.6.6 Electropermeabilization cell with rotating electrodes

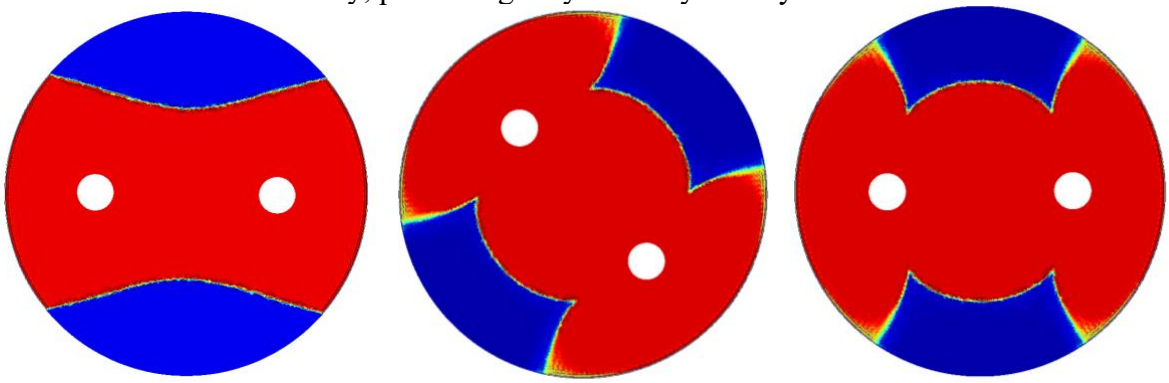
In the conceptual model presented below, the rotation frequency is 1.3 Hz, in the counterclockwise direction. Electrode rotation temporally homogenizes field exposure, significantly reducing non-permeabilized regions and accelerating the attainment of the target state, while maintaining a controlled thermal effect [15].



t = 0 s. t = 9,9 s. t = 10 s.

Fig. 5.19 – Numerical simulation results: electric field represented by field lines and normalized vectors (electric field intensity), together with equipotential curves. Rotating circular cell.

Figure 5.19 shows the electric field for the rotating cell at different time instants. From the initial moment, when the field lines are symmetric with respect to the two planes of geometric symmetry, up to t = 10 s, when the same configuration is recovered, the field structure evolves continuously, preserving only centrosymmetry.



t = 0,005 s; σ_{max} = 0,001 S/m. t = 1 s; σ_{max} = 0,119 S/m. t = 10 s; σ_{max} = 0,129 S/m.

Fig. 5.20 – Numerical simulation results: electrical conductivity gradient, where the red region corresponds to the permeabilized zone and the blue region to the non-permeabilized zone. Rotating circular cell.

Figure 5.20 presents the electrical conductivity distribution for the rotating cell at different time instants. It can be observed that the still non-permeabilized region progressively decreases as the EP threshold is reached.

5.6.7 Conclusions

Pulsed electric field (PEF)–assisted extraction is based on electroporation, a phenomenon in which exceeding a critical transmembrane voltage threshold induces pore formation and reduces the diffusion barrier. The consequence is accelerated mass transfer at low temperatures, while preserving volatile and thermosensitive compounds. Depending on the field amplitude, electroporation may be reversible or irreversible, providing a continuous operational window ranging from permeability enhancement to complete cellular disruption.

Permeabilization efficiency is governed by the electric pulse parameters and by the electrical and geometric properties of the matrix. The synthesized results indicate that bipolar rectangular pulses achieve the same degree of permeabilization at lower electric-field amplitudes, confirming the role of effective time above threshold and field inversion in reducing undesired effects. Joule heating can be controlled via PWM regimes with low duty cycles and active cooling; however, in burst operation, the frequency–temperature dependence is nonlinear, necessitating fine-tuning to prevent thermal accumulation.

Coupled simulations of the electric field, variable electrical conductivity, and heat transfer highlight the persistence of sub-threshold regions, whose reduction by increasing the applied voltage is limited by matrix degradation thresholds. In this context, cell geometry and electrode architecture become decisive. Elliptical cross-sections and electrode rotation improve the uniformity of the effective electric field, reducing non-permeabilized regions without inducing significant thermal effects.

The simplifying assumptions of the model—linear medium, piecewise homogeneous behavior, constant properties within each phase, and neglect of induced thermal convection—do not alter the overall conclusion. PEF system design must be carried out along three axes: waveform optimization, system geometry, and thermal management.

In conclusion, PEF represents a robust and selective intensification technology for extraction: by controlling pulse shape and parameters, combined with geometric optimization and thermal management, uniform permeabilization can be achieved at lower electric-field intensities.

Chapter 6
Extraction in an ultrasonic field

This chapter presents ultrasound-assisted extraction and the ultrasound (US) sources employed. The operating principles of piezoelectric and magnetostrictive transducers are described, with emphasis on the piezoelectric effect and energy-conversion efficiency.

The chapter further details the role of the sonotrode in energy transfer and focuses within the liquid medium, as well as the parameters governing permeabilization and mass transfer. Finally, numerical modeling and analysis of the assembly are presented.

6.1 US sources used in the extraction process

Sound is a mechanical wave that propagates through solid, liquid, or gaseous media. The human ear perceives frequencies in the range of 16 Hz–16 kHz and intensities between 10^{-12} W/m² and 10^{2} W/m² [32]. Waves whose frequency exceeds the upper limit of audible sound are referred to as ultrasound (US), while frequencies above 10^{10} Hz are classified as hypersound (HS).

Ultrasound exhibits the following characteristics: the transmitted energies are higher than in the case of audible sound; absorption and scattering of US are more pronounced compared to sound in the same reference medium; US transmission is directly proportional to the density of the propagation medium; and ultrasound waves propagate with high acceleration.

The propagation of ultrasound in a liquid medium is accompanied by cavitation, namely the rapid formation and violent collapse of vapor-filled bubbles within the liquid. Depending on the ultrasound frequency, vapor bubbles exhibit different dynamic behaviors. The speed of sound-wave propagation depends on the properties of the medium, such as density and compressibility [33].

$$C = \sqrt{\frac{1}{\rho\beta'}}, \tag{55}$$

where β [m^3/Pa] is the compressibility at constant temperature.

Waves may be longitudinal (particle displacement in the direction of propagation) or transverse (in solids, particle displacement perpendicular to the direction of propagation).

Ultrasound is used in numerous fields (medicine, chemistry, materials science, engineering). In practice, low frequencies (tens of kHz) are commonly employed for cleaning, welding, and machining, while medium frequencies (hundreds of kHz to MHz) are used for emulsification and flaw detection [16].

6.1.1 Piezoelectric effect

This subsection presents the ultrasound device, the structure of the silicon crystal in equilibrium and under dipole formation, the electrical, mechanical, and thermal parameters, as well as the equations describing piezoelectric effects.

Figure 6.1 illustrates the components of an ultrasound apparatus that can be used for ultrasound-assisted permeabilization of cellular membranes in organic media [34].

The device transmits electrical signals to the piezoelectric transducer, which generates ultrasound that is subsequently propagated into the fluid medium through the sonotrode in which it is immersed. The frequency, amplitude, and duration of the electrical signals are controllable process parameters. The operation of the piezoelectric transducer is based on the piezoelectric effect, a property of dielectric materials to deform when subjected to an electric

field. This effect is reversible, as piezoelectric materials generate an electric field when mechanical forces are applied to them [174].

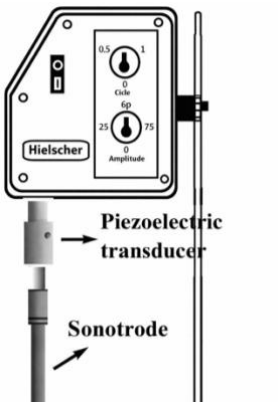


Fig. 6.1 - Schematic diagram of the UP200S ultrasonic device (200 W, 24 kHz) [34].

Piezoelectricity is generated by certain dielectric materials (quartz, PZT piezoceramics).

In a qualitative interpretation of the electrical polarization state, at rest (in the absence of electric or mechanical excitation), the atoms of the piezoelectric crystal form two equilateral triangles with common centers ($Q^- = Q^+$). When the crystal is mechanically loaded (tension or compression), the centers of the two triangles separate from each other ($Q^- \neq Q^+$). This phenomenon is equivalent to the formation of an electric dipole and, consequently, to the generation of an electric potential gradient (spatial variation) [16].

Electrical parameters: relative dielectric constant [–], piezoelectric strain coefficient [m/V], piezoelectric voltage coefficient [V·m/N], electromechanical coupling coefficient [–], polarization electric field [V/m], coercive electric field [V/m].

Mechanical parameters: mass density [kg/m³], elastic modulus [N/m²], compressive stress [N/m²], tensile stress [N/m²].

Thermal parameters: thermal expansion coefficient [1/K], specific heat capacity [J/kg·K].

$$\mathbf{P} = d\boldsymbol{\sigma}, \tag{56}$$

$$\mathbf{x} = g\mathbf{P}. \tag{57}$$

Equation (56) relates the electric polarization $\mathbf{P}$ [C/m²] to the normal mechanical stress $\boldsymbol{\sigma}$ [N/m²], introducing the proportionality factor d [C/N], and characterizes the direct piezoelectric effect. Equation (57) relates the elastic strain $\mathbf{x}$ [–] to polarization using the piezoelectric coefficient g [m³/C] and represents the inverse piezoelectric effect.

The temporary electric polarization is given by the constitutive relation between $\mathbf{D}$, $\mathbf{E}$, and $\mathbf{P}$, in the form

$$\mathbf{P} = \varepsilon_0(\varepsilon_r - 1)\mathbf{E}, \tag{58}$$

where $\boldsymbol{D}$ [C/m²] is the electric displacement, $\boldsymbol{E}$ [V/m] is the electric field intensity, ε_r [–] is the relative electric permittivity, and ε_0 [F/m] is the electric permittivity of free space (air).

Equation (58) becomes:

$$\mathbf{x} = g\mathbf{P} = g\varepsilon_0(\varepsilon - 1)\mathbf{E} = d\mathbf{E}. \tag{59}$$

6.1.2 Piezoelectric converter

A piezoelectric element supplied with an alternating electric voltage primarily ensures the conversion of energy from electrical form into mechanical form (mechanical vibrations).

The conversion efficiency depends on internal and external losses, as well as on tuning to the assembly's mechanical resonance. Near the resonance frequency, material displacements increase significantly, whereas at frequencies far above resonance, they decrease rapidly. Common materials (PZT, AlN, PVDF) offer trade-offs between robustness, cost, and processability. Piezoceramics generally provide higher overall efficiency and better thermal stability than alternative magnetostrictive solutions for the same acoustic power [17].

The process of acoustic cavitation formation in the working fluid medium begins with the electric generator, which must be synchronized with the mechanical resonance frequency of the desired operating domain, while the generator frequency is matched to the fundamental frequency of the piezoelectric material [17].

Operation below the resonance frequency produces deformation of the piezoelectric element that is nearly frequency-independent and proportional to the applied force. Near the resonance frequency, the deformation amplitude doubles compared to the nominal value (Fig. 6.6). A piezoceramic material should not be allowed to deform by more than 500×10^{-6} m/m [17].

The electromechanical coupling coefficient of the piezoelectric element is given by [16]

$$k = (E_m/E_e)^{1/2},. \tag{61}$$

where E_m is the mechanical energy

$$E_m = \frac{1}{2} Y S^2 V, \tag{62}$$

E_e is the electrical energy,

$$E_e = \frac{1}{2} C U^2, \tag{63}$$

and S [–] is the strain, V [m³] is the volume of the piezoelectric element, Y [Pa] is Young's modulus, C [F] is the electrical capacitance, and U [V] is the applied electrical voltage at the terminals.

6.1.3 Magnetostrictive converter

Magnetostrictive transducers use a ferromagnetic core excited by a coil, in which a time-varying magnetic field induces periodic linear displacements (magnetostriction) that generate the acoustic wave.

Due to the conversion chain (electrical–magnetic–mechanical–acoustic) and Joule losses, the overall efficiency is generally lower than that of piezoelectric transducers at comparable power levels [18].

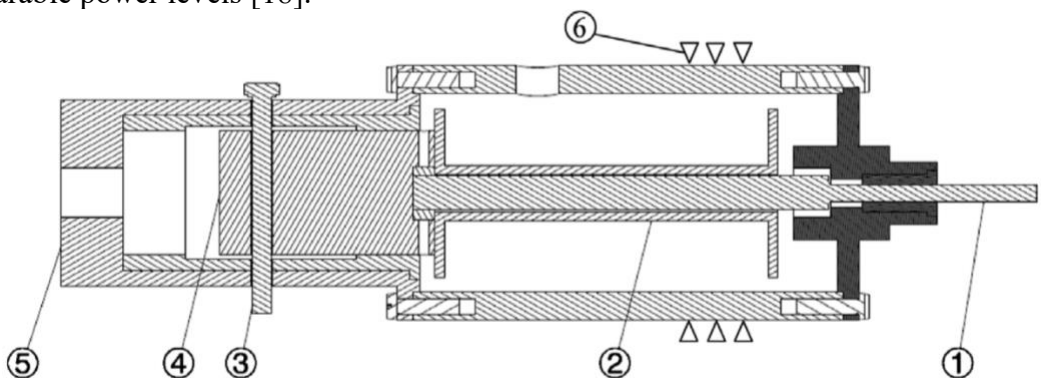


Fig. 6.9 – Magnetostrictive transducer: 1 – rod, 2 – coil, 3 – fastening screw, 4 – support, 5 – aluminum housing, 6 – mounting bracket [18].

The calculation of the vibration of the translational element is given by

$$[\frac{\partial M}{\partial z} dz = I \frac{\partial^2 \varphi}{\partial t^2}, \tag{64}$$

where M [N·m] is the torque, I [kg·m²] is the moment of inertia, $\varphi(z,t)$ [rad] is the angular displacement, and t [s] is time.

6.2 Use of US waves in extraction

The sonotrode (mechanical element) transfers and focuses mechanical vibrations through ultrasound–liquid interaction, which produces cavitation, heating, and pressure,

processes required for permeabilization and disruption of the plant matrix. The materials used for sonotrode fabrication (tool steel, titanium) and anti-wear coatings (titanium nitride) are selected to withstand mechanical and thermal stresses. The shape and dimensions of the sonotrode tip (flat, cylindrical, or stepped) govern acoustic coupling and energy distribution.

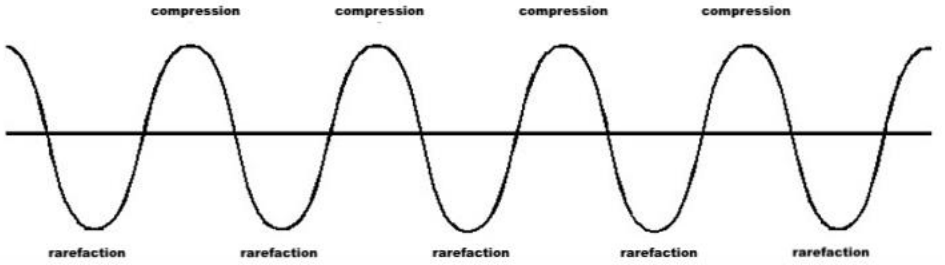


Fig. 6.12 – Process of microcavitation formation in a liquid, qualitative representation [35].

Cavitation—considered at a later stage of the research—is generated by ultrasound waves that alternately compress (increase density) and rarefy (decrease density) the medium through which they propagate; this phenomenon is qualitatively illustrated in Fig. 6.12. Ultrasound-wave propagation occurs in a liquid medium; in the proposed case, the properties of water are used for the working fluid.

Organic cell membranes may exhibit a refractory transmembrane voltage drop of 50-200 mV, with the inside of the cell at a negative potential. Based on these data, the order of magnitude of the electrical resistance of the membrane can be estimated:

$$U_M = E_G + IR, \tag{66}$$

where U_M [mV] is the transmembrane electric voltage drop, E_G [mV] is the Goldman equilibrium potential, I[nA] is the transmembrane electric current, and R [kΩ] is the electrical resistance of the membrane, with $R = 2.1$ kΩ for the cellular membrane [36].

6.3 US-assisted extraction process

This subsection presents the numerical analysis of the piezoelectric ultrasound (US) source, along with the physical model and computational domain, used to determine both the natural and resonance frequencies. The four coupled problems—(1) structural/piezoelectric (sonotrode); (2) ultrasound propagation (fluid medium inside the cell); (3) forced flow in the working fluid (cell); and (4) heat transfer—are numerically integrated in three stages: (a) the structural/piezoelectric problem (sonotrode); (b) ultrasound propagation (cell); and (c) fluid motion and heat transfer (cell).

From an electrical standpoint, cells exhibit a refractory transmembrane potential difference (tens to hundreds of mV). From a mechanical perspective, permeabilization occurs when local forces exceed the membrane strength threshold. In practice, control of sonication frequency, amplitude, and duration is essential to deliver the required acoustic force without inducing thermal degradation.

6.3.1 Piezoelectric ultrasound source

The sonotrode functions as a coupling and conversion element: one end is attached to the ultrasound transducer, while the other is immersed in the working medium [19].

Following the presentation of the electromechanical conversion chain and impedance matching, the next logical step is to analyze the interaction between ultrasound and the extraction medium. At approximately 26 kHz and appropriate amplitudes, the acoustic field induces cavitation, whose intensity depends on solvent properties (surface tension, viscosity, vapor pressure), temperature, and solid loading (particle-size distribution). These variables

control bubble density and dynamics, and their collapse generates microjets and shock waves that disrupt the matrix, thin the diffusive boundary layer, and accelerate mass transfer. The spatial distribution of these effects is governed by vessel geometry, the assembly's acoustic tuning, and the tip-to-wall distance, which may lead to standing waves and "dead zones."

In the numerical analysis performed, ultrasound permeabilization is decomposed to clearly decouple two physical phenomena: local nonlinear microphenomena at the ultrasound–extraction medium interface and the distribution of the ultrasonic field within the vessel. This approach reduces computational effort and cost (across different mesh resolutions and time steps), ensures convergence and numerical stability, and enables calibration and validation against datasets specific to each type of physical phenomenon.

6.3.2 Sonotrode analysis

This subsection presents the numerical modeling and the transducer's electromechanical response (electric field and deformations), identifying the natural frequencies and resonances relevant to extraction. An axisymmetric model was employed, with PZT layers connected in parallel and represented by an equivalent resistance–capacitance circuit.

Accounting for the sonotrode mass reduces natural frequencies and maximum displacements. The transient stabilization regime for sinusoidal excitation at resonance (on the order of tens of kHz) lasts several hundred periods. The applied voltage amplitude must be adjusted to remain within allowable deformation limits [20–22].

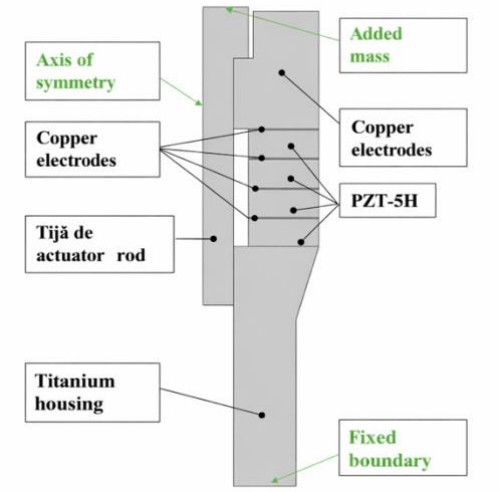


Fig. 6.16 – Simplified, axisymmetric computational domain and components of the piezoelectric device [37].

6.3.3 Integration of the sonotrode with the extraction cell

This subsection presents the linear piezoelectric actuator and the vessel containing the mixture (solvent + vegetal suspension). The analysis is staged as follows: (1) the structural/piezoelectric response of the sonotrode; (2) ultrasound propagation within the cell (steady harmonic regime); (3) acoustically induced flow (Navier–Stokes equations, transient regime) and heat transfer.

The pressure generated by the sonotrode becomes a boundary condition for the acoustic domain, while the acoustic intensity is transformed into a source term for the fluid domain [23]. The numerical computation is performed based on the constitutive piezoelectric relations, expressed in the mechanical stress–electric field formulation [37]:

$$\begin{cases} \mathbf{T} = \mathbf{c}_{\mathrm{d}}\mathbf{S} - \mathbf{q}^{\mathrm{T}}\mathbf{D}, \\ \mathbf{E} = -\mathbf{q}\mathbf{S} + \boldsymbol{\varepsilon}_{\mathrm{S}}^{-1}\mathbf{D}', \end{cases} \tag{67}$$

where $\mathbf{T}$ [N/m²] is the mechanical stress vector, $\mathbf{c_d}$ [N/m²] is the mechanical stiffness matrix, $\mathbf{S}$ is the mechanical strain vector, $\mathbf{q}^T$ [N/C] is the matrix of piezoelectric coupling coefficients, $\mathbf{D}$ [C/m²] is the electric displacement, $\mathbf{E}$[V/m] is the electric field intensity, and εs [F/m] is the electric permittivity at constant strain.

The mathematical model is completed by the electromagnetic field laws [37]:

Electric charge conservation $$\nabla \cdot \mathbf{J} = \mathbf{0}, \tag{68}$$

Electrical conduction $$\mathbf{J} = \sigma\mathbf{E}, \tag{69}$$

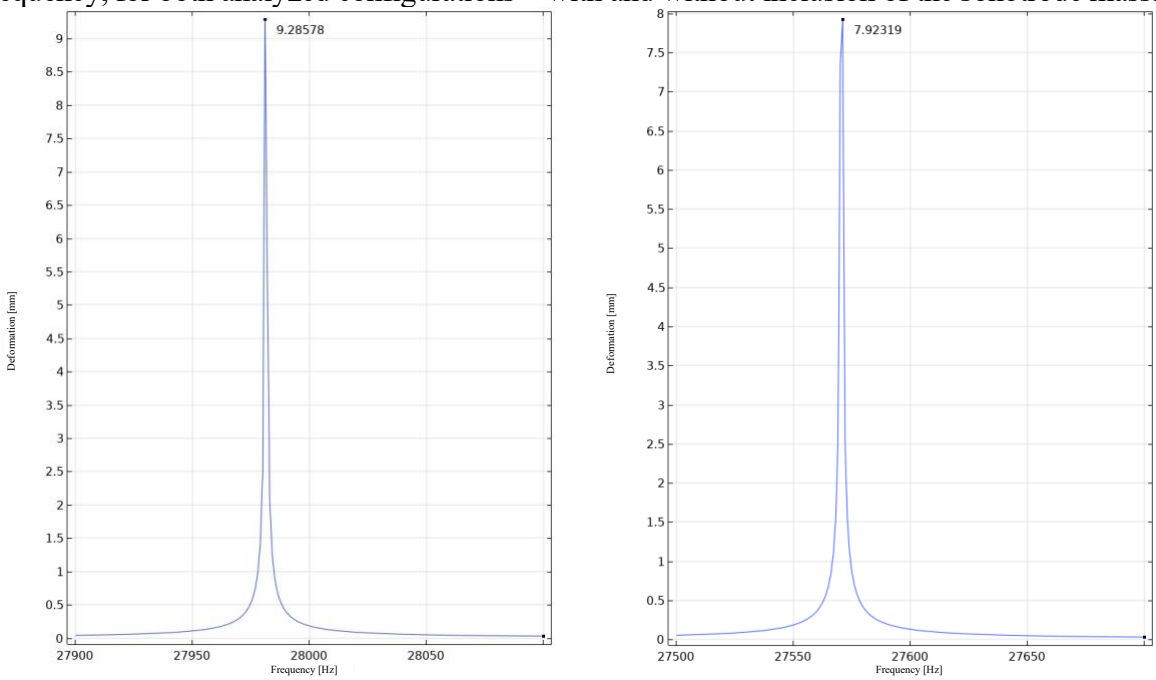
Electric flux $\nabla \cdot \mathbf{D} = \rho_v,$ (70)

Consequence of electromagnetic induction $\mathbf{E} = -\nabla \mathbf{V},$ (71)

Constitutive (material) law $\mathbf{D} = \varepsilon \mathbf{E} + \mathbf{P},$ (72)

where J [A/m²] is the electric current density, σ [S/m] is the electrical conductivity, ρ_v [C/m³] is the volumetric electric charge density, V [V] denotes the electric potential, and **P** [C/m²] is the electric polarization.

Figure 6.19 illustrates the variation of the actuator rod displacement as a function of frequency, for both analyzed configurations—with and without inclusion of the sonotrode mass.



a. without the sonotrode mass, $d_{\max} = 9.29$ mm. b. with the sonotrode mass, $d_{\max} = 7.92$ mm.

Fig. 6.19 – Maximum axial displacement of the actuator rod as a function of frequency [37].

6.3.3 Integrarea sonotronului cu celula de extracţie

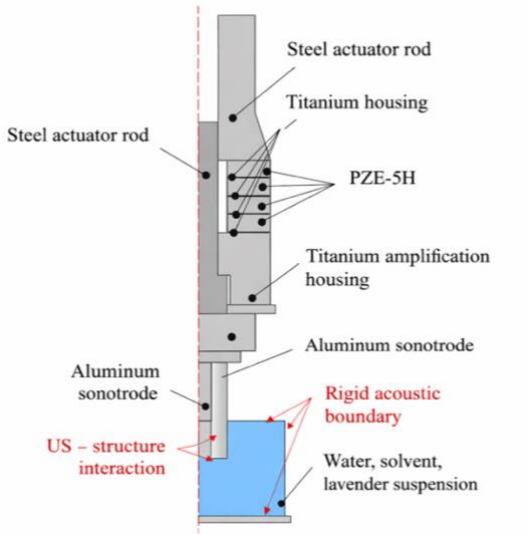


Fig. 6.21 – PZE US linear motor and working vessel [22].

This subsection presents the two-dimensional (2D) axisymmetric computational domain of the assembly, consisting of the linear actuator and the working vessel containing the mixture of water, solvent, and lavender flower suspension. All structural components of the assembly are highlighted, together with the boundary conditions (indicated by red arrows) corresponding to the problem describing the interaction between the ultrasonic field and the working fluid.

The numerical analysis is performed in a steady-state harmonic regime for the acoustic pressure and piezoelectric coupling problems, and in a transient regime for the flow within the working vessel.

The natural frequencies and the resonance frequency of the device are determined. At this frequency, the steady-state harmonic regime is adopted, and the actuator's operation is

evaluated acoustically, including ultrasound transmission and the induced fluid motion within the working vessel.

6.3.4 Modeling of the processes occurring in the ultrasound extraction cell

This subsection presents the results obtained from coupling the three physical phenomena: ultrasound propagation, fluid motion, and heat transfer within the cell.

The mathematical model describing the operation of the piezoelectric linear ultrasound motor in a steady-state harmonic regime is expressed as [22]:

$$\nabla \cdot \left(-\frac{1}{\rho_0}\nabla p\right) - \frac{\omega^2 p}{\rho_0 c_s^2} = 0, \tag{73}$$

where p [Pa] is the acoustic pressure, c_s [m/s] is the speed of sound in the fluid medium, ρ_0 [kg/m³] is the mass density, and ω [rad/s] is the angular frequency of the sound wave. The boundary conditions for this quasi-stationary problem are shown in Fig. 6.21 (marked in red).

The fluid-flow problem in the working vessel is described by the Navier–Stokes equations (Newtonian fluid, incompressible flow, transient regime), corresponding to momentum and mass conservation:

$$\frac{\partial \mathbf{u}}{\partial t} + (\mathbf{u}\cdot\nabla)\mathbf{u} = -\nabla p + \mu\Delta\mathbf{u} + \mathbf{f}, \nabla\cdot\mathbf{u} = 0, \tag{75,76}$$

where $\mathbf{u}$ [m/s] is the fluid velocity in the working vessel, μ [Pa·s] is the dynamic viscosity, p [Pa] is the pressure, and $\mathbf{f}$ [N/m³] is the body-force density induced by the intensity of the ultrasound wave,

$$\mathbf{f} = \frac{2\alpha}{c_s}\mathbf{I}, \tag{77}$$

where α [Np/m] is the attenuation coefficient of the liquid medium and $\mathbf{I}$ [W/m²] is the intensity (power) of the ultrasound wave.

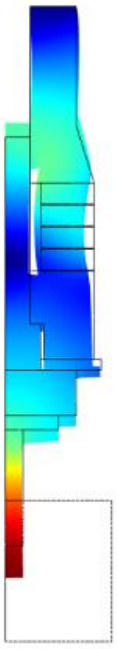


Fig. 6.22 – Deformation of the sonotron, $f_{r3} = 28.520$ kHz [22].

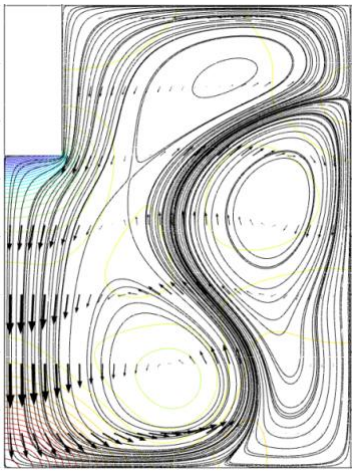


Fig. 6.23 – Flow field, isobars, and streamlines at $t = 900$ s [22].

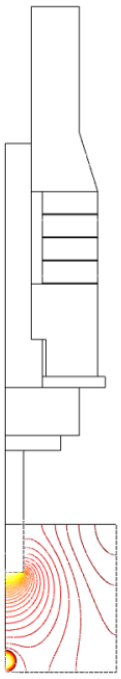


Fig. 6.24 – Temperature field at $t = 900$ s [22].

Figure 6.22 illustrates the deformation field of the linear piezoelectric ultrasound motor at the resonance frequency $f_{r3} = 28.520$ kHz. Among the obtained values, the highest

resonance frequency is selected, as it enables a more efficient, higher-quality extraction process by preserving a greater number of volatile components, albeit at a longer extraction duration [22].

Figure 6.23 presents the flow streamlines inside the working vessel at a given time instant. It is observed that the final time interval used in the extraction process is insufficient to allow flow stabilization and the attainment of a steady-state regime for the Navier–Stokes problem associated with the fluid in the working vessel.

As time progresses, the flow structure becomes better defined, and the distribution of isobars highlights the fluid's progressive stabilization. The thermal analysis of the ultrasound-assisted extraction process requires solving the energy equation,

$$\rho_0 C_p \left(\frac{\partial T}{\partial t} + (\mathbf{u} \cdot \nabla)\mathrm{T}\right) = k\nabla^2\mathrm{T} + \dot{Q}, \tag{78}$$

where C_p [J/kg·K] is the specific heat capacity, k [W/m·K] is the thermal conductivity, and $\dot{Q}$ [W/m³] is the ultrasound heat source.

The boundary conditions are insulating on all sides of the computational domain. The initial state is isothermal (20 °C).

Figure 6.24 highlights the evolution of the isothermal distribution within the cell at time s, where the temperature distribution exhibits more pronounced gradients; however, the system remains quasi-isothermal (at 40 °C).

6.4 Conclusions

The efficiency of ultrasound-assisted extraction is governed by cavitation and acoustic resonance during sound-wave propagation in liquid media. Gas-bubble dynamics generate microjets and shock waves that disrupt the matrix, reduce the diffusive boundary layer, and accelerate mass transfer. Vessel design, acoustic tuning, and the distance between the sonotrode tip and vessel walls determine US field distribution; standing waves and low-energy regions may occur, requiring architectural optimization.

For extraction applications, piezoelectric transducers are preferred over magnetostrictive transducers due to higher efficiency, lower Joule losses, and greater precision in frequency and amplitude control. Safe operation requires compliance with piezoceramic deformation limits (~5×10^{-4} m/m) and operation near, but below, the mechanical resonance to maximize energy transfer without damaging the transducer.

The linear piezoelectric US motor consists of an amplifying housing and a sonotrode that focuses acoustic energy into a working cell containing water, solvent, and lavender suspension. The assembly is modeled as a linear, homogeneous, and isotropic medium for ultrasound propagation, induced flow, and heat transfer. The sonotrode, typically made of steel or titanium, ensures impedance matching and mechanical amplification, with its geometry optimized to maximize power density and minimize low-energy zones.

The coupled interaction of the piezoelectric, acoustic, fluid-flow, and thermal fields is analyzed numerically through a staged multiphysics approach. Results show that including the sonotrode mass reduces the resonance frequency and deformation amplitude, necessitating fine adjustment of the excitation voltage (400 V in all cases). A two-dimensional axisymmetric model is used to identify natural frequencies and the optimal resonance for coupling with the working vessel.

Although the fluid-dynamics model assumes constant properties for the permeabilized phase, the results demonstrate that a PZT-5H transducer tuned to ~28.5 kHz, combined with an impedance-matched sonotrode and controlled excitation, enables rapid, selective, and reproducible extraction while preserving volatile compounds. With appropriate processing time, thermal monitoring, and adherence to mechanical and electrical limits, this approach provides a solid framework for industrial scale-up.

Chapter 7
Conclusions

This chapter presents the results obtained, the original contributions, the directions for future development, the list of publications produced during the doctoral studies, and the thesis conclusions.

The thesis examined the transition from scientific and industrial motivations for intensifying the extraction of bioactive compounds to the theoretical foundation, multiphysical numerical modeling, and energy integration of extraction installations, including the demonstration of photovoltaic power supply and thermal management.

Modern technologies—pulsed electric fields (PEF), microwaves (MAE), and ultrasound (UAE)—can operate as direct extraction methods, significantly reducing processing times and improving product quality compared to conventional techniques.

The decisive factor is not only the amount of energy introduced, but also its spatio-temporal distribution and the removal of unwanted energy through thermal control.

PV/T integration can autonomously support laboratory- and pilot-scale installations, enable useful heat recovery, and improve the electrical performance of photovoltaic panels.

The transition to electromagnetic and electromechanical technologies is justified based on processing time, specific energy consumption, and product quality. The studied matrices (coffee and lavender) are economically relevant and sensitive to processing regimes.

7.1 Obtained results

Classical separation methods (sedimentation, centrifugation, steam distillation, liquid–liquid extraction) rapidly approach their productivity limits. Among extraction processes, PEF, MAE, and UAE offer significantly shorter processing times while maintaining yields that are at least comparable. For lavender, MAE yields are comparable to those of hydrodistillation within minutes (rather than tens of minutes), whereas for coffee, it reduces processing times from hours to minutes. UAE, combined with polar solvents, increases mass flux through controlled cavitation.

For the numerical modeling of PEF, the electric field dependent on medium properties (σ, ε), the evolution of electrical conductivity (pore opening and resealing), and Joule heat transfer were coupled, including deformable FEM meshes. Sub-threshold regions ($E < E_{critic}$) were identified as persistent, leading to the development of two effective solutions: an elliptical cell geometry, which promotes electric-field redistribution, and electrode rotation, which progressively exposes the volume to field values $E > E_{critic}$. At the same time, appropriate power adjustment maintains an almost isothermal regime.

The PV/T energy integration was evaluated for three configurations: (S_0) natural convection, (S_1) active cooling with a single coil, and (S_2) a counter-flow heat exchanger.

Under natural convection, the panel reaches approximately 99 °C, which is unfavorable for electrical conversion. Solution (S_1) reduces the panel temperature to around 23 °C with moderate pumping effort, while (S_2) maximizes heat removal and electrical efficiency at the expense of increased hydraulic cost. Pulsed operation minimizes auxiliary consumption while maintaining intermediate panel temperatures of 56–57 °C. These results indicate that PV/T architectures can support the power supply of mobile or autonomous PEF, UAE, and MAE equipment.

Ultrasound simulations that couple piezoelectric excitation, the acoustic field, fluid flow, and heat transfer confirm that attaching the sonotrode reduces the resonance frequency and deformation amplitude, necessitating fine adjustment of the excitation voltage. From a thermal standpoint, the system remains nearly isothermal but requires careful thermal insulation management.

The transition toward reproducible industrial solutions is conditioned by coherent multiphysics design, control of energy distribution within the sample, and energetic integration of subsystems. In this context, modular PEF and UAE lines powered by PV/T systems are technically feasible.

7.2 Original contributions

Off-grid PV energy architecture [10,11], with sizing criteria that correlate consumption (PEF / UAE) [20–23], local irradiance, storage capacity, and MPPT / inverter efficiencies within a unified decision-making workflow.

Analytical model for PV panel thermal loading: Nu–Ra correlations incorporating solar geometry, $\mathrm{Nu}_L(\mathrm{Ra}_L^*, \varphi)$ charts and h(φ) curves for CFD initialization and passive optimization (tilt angle) [10,11].

Three-dimensional (FEM) thermo-hydrodynamic numerical model of a PV/T system with rear heat exchanger, including scenarios S_0, S_1, and S_2, and maps of $\dot{Q}$, T_{PV}, $\dot{W}$, and Re_D, as well as transition thresholds and $\dot{Q}/\dot{W}$ trade-offs [10,11].

Pulsed cooling strategy (T_{start}, T_{stop}) that drastically reduces pump operating time while maintaining the PV panel within a prescribed thermal range [11].

Techno-economic guideline for S_1 vs. S_2 (maximum PV efficiency vs. hydraulic cost), together with unified indicators $\eta(T_{PV})$ and $\dot{Q}/\dot{W}$ for scaling and optimization [10,11].

Electromagnetic–thermal coupling through field-dependent material properties, explicit treatment of the critical field threshold E_{critical} in the dynamics of $\sigma(x,t)$, and inclusion of rotational motion together with thermal-regime analysis within the extraction cell [15].

7.3 Development directions

Advanced control: coordination of MPPT with cooling (continuous/pulsed) via predictive strategies (thermal limits, minimization of auxiliary energy, irradiance forecasting).

Coupling to useful thermal loads (solvent preheating, sanitization, drying) or to micro-Stirling engines.

Functional surfaces: selective IR coatings, controlled emissivity, optimized thermal interfaces, and assessment of their impact on efficiency and durability.

Integrated digital twin (thermo–electro–hydraulic + extraction), enabling multi-objective optimization (CAPEX / OPEX, $\dot{Q}/\dot{W}$, MPPT, LCA / CO_2-eq) and design maps adapted to latitude and operating scenarios.

For PEF: bipolar/trapezoidal waveforms, burst regimes, anti-fouling electrodes, impedance, and temperature monitoring with adaptive control.

For UAE: multi-frequency networks (20–40–80 kHz), cavitation management, dynamic acoustic matching, and correlation of acoustic power with extraction yield across different matrices.

Hybrid sequences (PEF–UAE, MAE–UAE) to combine rapid permeabilization with mechanical detachment.

Standardization and compliance: EMC/EMI, electrical safety, GMP/HACCP.

Energy integration at scale: DC microgrids, electrical and thermal storage, peak-load management.

Comprehensive LCA / TCO: water and solvent footprint, residual biomass valorization, and circular-economy scenarios.

7.4 List of published works

1. F. Săftoiu, A. M. Morega, Cooling System for Photovoltaic Panels, Revue Roumaine des Sciences Techniques – Série Électrotechnique et Énergétique, vol. 67, nr. 3, pp. 343–348, 2022. ISSN: 0035-4066; Editor: Romanian Academy. WOS: 000870731700020.
2. F. Săftoiu, A. M. Morega, Pulsed Cooling System for Photovoltaic Panels, The 13th International Symposium on Advanced Topics in Electrical Engineering (ATEE 2023), Bucharest, Romania, 23–25 Mar. 2023, pp. 1–5. IEEE Explore.
3. Y. Veli, F. Săftoiu, A. M. Morega, Analiza Numerică a unui Traductor Piezoelectric de Ultrasunet, Actualități și Perspective în Domeniul Mașinilor Electrice (APME/SME), Vol. 19, nr. 1, pp. 52–57, 2023. ISSN: 1843-5912; DOI: 10.36801/apme.2023.1.7.
4. Y. Veli, F. Săftoiu, A. M. Morega, Predimensionarea unui Traductor Piezoelectric De Ultrasunet, Actualități și Perspective în Domeniul Mașinilor Electrice (APME/SME), București, 2023. (SME 663).
5. Y. Veli, F. Săftoiu, A. M. Morega, Interaction of Ultrasonic and Heat Flow in Essential Oil Extraction – A Constructal Glimpse, 14th Constructal Law Conference – Design in Nature and Evolution, Bucharest, 10 – 11 Oct. 2024, pp. 175–178. DOI: 10.59277/CLC.2024.44, ISSN: 3061-6239, ISBN: 978-973-27-3918-1.
6. F. Săftoiu, Y. Veli, A. M. Morega, Electropermeabilization For Organic Material – Numerical Modeling, Revue Roumaine des Sciences Techniques - Série Électrotechnique et Énergétique, nr. 4, Editor: Romanian Academy, vol. 70, pp. 603–608, Nov. 2025, DOI: 10.59277/RRST-EE.2025.4.28. WOS: 001627001400026.
7. Y. Veli, F. Săftoiu, A. M. Morega, Structural optimization of a piezoelectric ultrasonic Transducer for permeabilization of organic materials, The 14th International Symposium on Advanced Topics in Electrical Engineering (ATEE 2025), Bucharest, Romania, IEEE Explore.

7.5 Final conclusion

The work demonstrates that the triad of **multiphysics design, fine control of energy distribution, and energy integration** enables the transformation of PEF, MAE, and UAE technologies from laboratory solutions into robust, scalable, and sustainable processes. This approach outlines modular extraction lines for applications such as lavender and coffee, powered by photovoltaic systems, in which PEF, MAE, and UAE stations operate at maximum efficiency and are supported by active thermal management.

The next step is pilot-scale validation under continuous operation, with simultaneous monitoring of the energy balance, extract composition, and operational stability, as a prerequisite for industrial transfer.

References (selection)

[1] K. Rusanov, P. Vassileva, M. Rusanova, I. Atanassov, “Identification of QTL controlling the ratio of linalool to linalyl acetate in the flowers of Lavandula angustifolia Mill var. Hemus”, Biotechnology & Biotechnological Equipment, vol. 37, no. 1, 2023.

[2] M. A. Vian, X. Fernandez, F. Visinoni, F. Chemat, “Microwave hydrodiffusion and gravity, a new technique for extraction of essential oils”, J. Chromatogr. A, vol. 1190, no. 1–2, pp. 14–17, 2008

[3] C. M. Tucker, “Coffee Culture: Local Experiences”, Global Connections, Routledge, 2017.

[4] UN. Secretary – General, World Commission on Environment and Development, ”Report of the World Commission on Environment and Development: Note / by the Secretary-General”, New York, 1987.

[5] W. G. García-Villalba, R. Rodríguez-Herrera, L. A. Ochoa-Martínez, O. M. Rutiaga-Quinones, M. G. Lopez, J. A. Gallegos-Infante, G. Bermúdez-Quinonesa, S. M. Gonzalez-Herrera, ”Comparative study of four extraction methods of fructans (agavins) from Agave durangensis: Heat treatment, ultrasound, microwave and simultaneous ultrasound-microwave”, 2023.

[6] J. H. Lienhard, V. Lienhard IV, ”A Heat Transfer Textbook”, 5th ed. Cambridge MA: Phlogiston Press, 2020.

[7] J. Nou, R. Chauvin, S. Thil, S. Grieu, “A new approach to the real-time assessment of the clear-sky direct normal irradiance”, Appl. Math. Model., vol. 40, 2016, doi: 10.1016/j.apm.2016.03.022.

[8] S. A. Saada, I. Kecili, R. Nebbali, “Preliminary study of a water cooled PV system”, in Proc. 2018 Int. Conf. Commun. Electr. Eng. (ICCEE), 2018, pp. 1–4.

[9] H.T. Lin, W.S. Yu, S.L Yang, ”Free convection on an arbitrarily inclined plate with uniform surface heat flux”, Wärme und Stofffübertragung, 24, pp.183-190, 1989.

[10] F. Săftoiu, A. M. Morega, ”Cooling System for Photovoltaic Panels”, Revue Roumaine des Sciences Techniques – Série Électrotechnique et Énergétique, vol. 67, nr. 3, pp. 343–348, 2022. ISSN: 0035-4066; Editor: Romanian Academy.

[11] F. Săftoiu, A. M. Morega, ”Pulsed Cooling System for Photovoltaic Panels”, The 13th International Symposium on Advanced Topics in Electrical Engineering (ATEE 2023), Bucharest, Romania, 23–25 Mar. 2023, pp. 1–5.

[12] T. Kotnik, W. Frey, M. Sack, S. Haberl Meglič, M. Peterka, D. Miklavčič, “Electroporation-based applications in biotechnology”, Trends Biotechnol., vol. 33, no. 8, pp. 480–488, Aug. 2015.

[13] F. Guo, X. Nie, J. Hong, Y. Zhang, J. Sun, “Influence of Joule heating during single-cell electroporation simulation under IRE and H-FIRE pulses”, Materials Today Communications, vol. 33, p. 104358, 2023.

[14] A. Çınar , K. Ateş , L.N.Ö. Polat , S. Elmasulu , I.K. Oğuz , O. Çınar, Ş. Özen, ”Adulteration control of lavender essential oil by using its electrical properties in the low-frequency range”, Measurement science review, 25, 3, pp. 141-147 (2025).

[15] F. Săftoiu, Y. Veli, A. M. Morega, ”Electropermeabilization for organic material – numerical modeling”, Revue Roumaine des Sciences Techniques - Série Électrotechnique et Énergétique, nr. 4, Editor: Romanian Academy.

[16] M. Scheffel, P. Știuca, ”Dispozitive cu ultrasunete. Ultrasunete. Caracteristici generale”, vol. I. Bucharest, Romania: Editura Tehnică, 1989.

[17] R. Carter, R. Kensley, ”Introduction to Piezoelectric Transducers”, Midé Technology Corp., Woburn, MA, USA, 2020.

[18] M. R. Karafi, Y. Hojjat, F. Sassani, M. Ghodsi, “A novel magnetostrictive torsional resonant transducer”, Sensors and Actuators A: Physical, vol. 195, pp. 71–78, 2013.

[19] https://www.hielscher.com/200ht_p.htm

[20] Y. Veli, F. Săftoiu, A. M. Morega, ”Analiza numerică a unui traductor piezoelectric de ultrasunet”, Actualități și Perspective în Domeniul Mașinilor Electrice (APME/SME), Vol. 19, nr. 1, pp. 52–57, 2023. ISSN: 1843-5912; DOI: 10.36801/apme.2023.1.7.

[21] Y. Veli, F. Săftoiu, A. M. Morega, ”Predimensionarea unui traductor piezoelectric de ultrasunet”, Actualități și Perspective în Domeniul Mașinilor Electrice (APME/SME), București, 2023. (SME 663).

[22] Y. Veli, F. Săftoiu, A. M. Morega, ”Interaction of Ultrasonic and Heat Flow in Essential Oil Extraction – A Constructal Glimpse”, 14th Constructal Law Conference – Design in Nature and Evolution, Bucharest, 10 - 11 Oct. 2024, pp. 175–178. DOI: 10.59277/CLC.2024.44.

[23] Y. Veli, F. Săftoiu, A. M. Morega, ”Structural optimization of a piezoelectric ultrasonic Transducer”, The 14th International Symposium on Advanced Topics in Electrical Engineering (ATEE 2025), Bucharest, Romania.

[24] A. LaPotin, K. L. Schulte, M. A. Steiner, K. Buznitsky, C. C. Kelsall, D. J. Friedman, E. J. Tervo, R. M. France, M. R. Young, A. Rohskopf, S. Verma, E. N. Wang, A. Henry, “Thermophotovoltaic efficiency of 40%”, Nature, vol. 604, no. 7905, pp. 287–291, Apr. 2022. doi: 10.1038/s41586-022-04473-y. [Online]. Available: https://www.ncbi.nlm.nih.gov/pmc/articles/PMC9007744

[25] K. Kurata, M. Matsushita, T. Yoshii, T. Fukunaga, și H. Takamatsu, “Effect of irreversible electroporation on three-dimensional cell culture model,” in *Proc. Annu. Int. Conf. IEEE Eng. Med. Biol. Soc. (EMBC)*, San Diego, CA, USA, 2012, pp. 179–182, doi: 10.1109/EMBC.2012.6345900.

[26] S. Najafian, *The effect of time and temperature on the shelf life of essential oils of Lavandula officinalis*, J. of Essential Oil Research, 28, 5, pp. 413-420 (2016).

[27] Comsol Multiphysics v. 5.6a, Release Notes (2021).

[28] E. Vorobiev, N. Lebovka, Pulsed-Electric-Fields-Induced Effects in Plant Tissues: Fundamental Aspects and Perspectives of Applications. In Electrotechnologies for extraction from food plants and biomaterials, Springer, New York, pp. 39-81, NY(2008).

[29] W. Milestone, Q. Hu, A. M. Loveless, A. L. Garner, R. P. Joshi, „Modeling coupledsingle cell electroporation and thermal effects from nanosecond electric pulse trains”, J. of Applied Physics, 132 (2022), 094701.

[30] K. A. DeBruin and W. Krassowska, “Modeling electroporation in a single cell: Effects of field strength and rest potential,” Biophys. J., vol. 77, no. 3, pp. 1213–1224, Sep. 1999. [Online]. Available: https://doi.org/10.1016/S0006-3495(99)76973-0.

[31] T. Kotnik, G. Pucihar, M. Rebersek, D. Miklavčič, and L. M. Mir, “Role of pulse shape in cell membrane electropermeabilization,” Biochim. Biophys. Acta, vol. 1614, no. 2, pp. 193–200, Aug. 2003. [Online]. Available: https://doi.org/10.1016/s0005-2736(03)00173-1.

[32] D. Purves, G. J. Augustine, D. Fitzpatrick, *et al.*, Eds., “The audible spectrum,” in *Neuroscience*, 2nd ed. Sunderland, MA, USA: Sinauer Associates, 2001.

[33] D. A. Ghersgal, V. M. Fridman, „Aparate cu ultrasunete.”, Bucharest, Romania: Editura Tehnică, 1962.

[34] T. Polachini, G. Carvalho, and J. Telis-Romero, “Determination of acoustic fields in acidic suspensions of peanut shell during pretreatment with high-intensity ultrasound,” Brazilian Journal of Chemical Engineering, vol. 34, pp. 385–394, 2017, doi: 10.1590/0104-6632.20170342s20150549.

[35] https://www.hielscher.com/ultrasonic-cavitation-in-liquids-2.html.

[36] M. Kates and L. A. Manson, Membrane Fluidity, Biomembranes, vol. 12. New York, NY: Plenum Press, 1984.

[37] **F. Săftoiu, A. M. Morega, Y. Veli, "Numerical analysis of a piezoelectric ultrasound transducer," Act. Perspect. Mach. Elect., vol. 19, no. 1, pp. 52–57, 2023. [Online]. Available: https://doi.org/10.36801.**